

Physical Modelling of Hydraulic Jump: Dynamic Properties and Internal Two-Phase Flow

Hang Wang

Ph.D. candidate, The University of Queensland, Brisbane, QLD 4103, Australia. Email: hang.wang@uqconnect.edu.au

Hubert Chanson

Professor, School of Civil Engineering, The University of Queensland, Brisbane, QLD 4103, Australia. E-mail: h.chanson@uq.edu.au

ABSTRACT: In a hydraulic jump, the turbulent flow region between the upstream supercritical flow and downstream subcritical flow is called the jump roller. The turbulence development in the jump roller leads to substantial energy dissipation as well as free-surface fluctuations, oscillations of jump position, air entrainment and unstationary velocity field. The time scales of these motions cover a broad range of frequencies, which may be critical to the design and maintenance of hydraulic structures. This paper presents a physical study of hydraulic jumps based upon a series of measurements of the free-surface and two-phase flow properties. Some long-term change in jump position was documented. The fluctuations of free-surface water level and longitudinal jump toe position were measured non-intrusively, corresponding to the relatively slow unstationary processes with frequency magnitude of about 1 Hz. Characteristic frequencies of these motions were reported, and the surface deformation pattern was characterised. The intrusive measurement of local void fraction and bubble frequency in the roller provided information on the turbulence properties corresponding to high frequency (greater than 10 Hz) processes. The air entrainment rate in the roller was calculated based on the void fraction and velocity distributions. The coupling between the free-surface position data and instantaneous void fraction revealed some interaction between the surface deformation and air entrainment process, though they were of different frequency magnitudes. The present study provided detailed physical description of the low- and high-frequency processes in hydraulic jumps. The understanding of these properties and their potential effects are fundamental to practical hydraulic engineering.

KEY WORDS: Hydraulic jump, Characteristic frequency, Free-surface, Air-water flow, Physical modelling.

1 INTRODUCTION

A hydraulic jump occurs in rivers or hydraulic structures where an open channel flow changes from a supercritical to subcritical flow motion. As the high-speed inflow impinges into a turbulent roller, substantial energy is dissipated and air is entrained. Figure 1(a) and 1(b) show a natural hydraulic jump at the end of a weir and an experimental hydraulic jump in a horizontal rectangular channel, both highlighting the intense turbulence and strong aeration. Although the hydraulic jump is usually treated as a steady flow, various pseud-periodic motions are noticed with a wide range of time scales. For example, the free-surface fluctuations, investigated by Mouaze et al. (2005), Kucukali and Chanson (2008), Murzyn and Chanson (2009) and Chachereau and Chanson (2011a), showed some characteristic frequencies roughly between 0.1 and 10 Hz. The oscillations of jump toe position and generation of large vortices in the roller were observed in a comparable time scale level (Zhang et al., 2013). Some long-term swing of jump position might also exist with much lower frequencies (Mossa, 1999). On the other hand, the turbulence properties associated with two-phase flow were studied based on much smaller time scales

(Chanson, 1995, 2007, 2010, Chanson and Brattberg, 2000, Murzyn et al., 2005, Chachereau and Chanson, 2011b). Though the time-averaged void fraction, bubble frequency and interfacial velocity distributions were well defined, it was believed that many turbulence properties were simultaneously affected by the low- and high-frequency fluctuations (Felder and Chanson, 2012). It is a challenge to fully understand these fluctuating features related to different physical processes which might interact with each other.

In the present study, hydraulic jumps were physically modelled with the inflow Froude number from 3.8 to 10 and the Reynolds number from 2.1×10^4 to 1.6×10^5 . The free-surface fluctuations were investigated non-intrusively using acoustic displacement meters, and the air-water flow properties were measured with an intrusive phase-detection probe. The results are presented according to the corresponding frequency levels: that is, the long-term jump position shift corresponding to the slowest motion, the free-surface properties corresponding to the low-frequency fluctuations, and the two-phase flow properties corresponding to the high-frequency turbulence. The work aimed to present new information leading to a better understanding on the processes of air entrainment, turbulence development and potential interactions in between.



Figure 1 (a) Hydraulic jump at Joe Sippel weir, Murgon QLD, Australia (5th March 2013) – $Q = 27.0 \text{ m}^3/\text{s}$, $B = 36.34 \text{ m}$, $Re = 7.3 \times 10^5$; (b) Experimental hydraulic jump – Flow conditions: $Q = 0.0812 \text{ m}^3/\text{s}$, $B = 0.5 \text{ m}$, $d_1 = 0.057 \text{ m}$, $x_1 = 1.25 \text{ m}$, $Fr_1 = 3.8$, $Re = 1.6 \times 10^5$.

2 PRESENTATION OF EXPERIMENTS

2.1 Experimental facility, instrumentation and data processing

Hydraulic jumps were modelled in a 3.2 m long, 0.5 m wide horizontal flume with smooth channel bed and glass sidewalls (Fig. 1(b)). Water was supplied by a constant head reservoir and the discharge was measured using Venturi meters. The flow conditions were controlled by an upstream undershoot sluice gate and a downstream overshoot gate. A sketch of experimental flow is shown in Figure 2, where h is the upstream gate opening, d_1 is the inflow depth immediately upstream the jump toe, x_1 is the longitudinal distance from the inlet to the jump toe and V_1 the average inflow velocity.

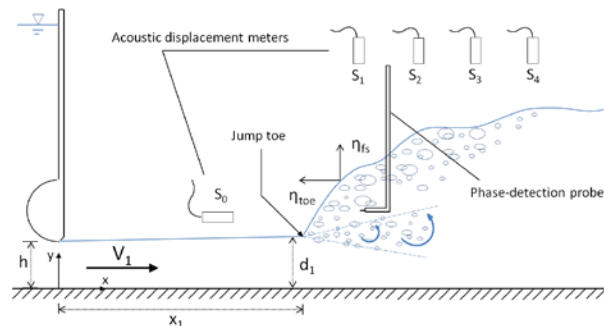


Figure 2 Sketch of experimental hydraulic jump and instrumental setup.

The long-term change of longitudinal jump position was observed by means of a high-definition

video camera (25 fps) through the channel sidewall. Frames were taken every 5 s for 160 minutes and the relative jump toe position $x-x_1$ was recorded.

The free-surface motions, including instantaneous water elevations and horizontal oscillations of the jump front, were recorded with a series of acoustic displacement meters (Microsonic™ Mic+25/IU/TC & Mic+35/IU/TC). The acoustic displacement meter emitted acoustic beams and received those reflected by the water surface. The distance between the sensor head and the water surface was derived from the travel time of the beam. In the present study, one displacement meter (S_0 in Fig. 2) was mounted horizontally over the inflow, with the sensor head facing the jump front from upstream. Another four displacement meters (S_1 to S_4) were placed vertically above the centreline of jump roller. All sensors were scanned at 50 Hz for at least 10 minutes. The voltage output signals were linearly converted into water elevations, referred to as η_{toe} and η_{fs} in horizontal and vertical directions respectively (Fig. 2).

A dual-tip phase-detection probe was used to detect the entrapped air bubbles or splashing droplets based upon the different electrical conductivities of air and water. At a given longitudinal position x in the roller and an elevation y above the bed, the phase-detection probe was sampled at 20 kHz for 45 s. The output voltage signals proportional to the conductivity level reflected the instantaneous void fraction. A single threshold was applied to convert the raw signal to a binary file in which 1 stood for air and 0 for water, and the time-averaged void fraction and bubble frequency were calculated. The two needle sensors ($\varnothing = 0.25$ mm) of the dual-tip phase-detection probe were separated by a longitudinal distance Δx_{tip} and they were designed to pierce a bubble or droplet. A cross-correlation between the signals of the two sensors provided a statistical measure for a known time lag τ . The interfacial velocity in the longitudinal direction was estimated as

$$V = \frac{\Delta x_{tip}}{T} \quad (1)$$

where T is the time lag for the maximum correlation coefficient: $T = \tau((R_{xx'})_{max})$, representing the interfacial travel time over the distance Δx_{tip} , and $R_{xx'}$ is the normalised cross-correlation coefficient. Assuming that the successive detection of air-water interfaces was a true random process, the turbulence intensity can be deduced as (Chanson and Toombes, 2002, Chanson and Carosi, 2007)

$$Tu = 0.851 \times \frac{\sqrt{\tau_{0.5}^2 - T_{0.5}^2}}{T} \quad (2)$$

for which $R_{xx'}(T+\tau_{0.5}) = (R_{xx'})_{max}/2$ and $R_{xx'}(T_{0.5}) = 0.5$, $R_{xx'}$ is the normalised auto-correlation coefficient of the leading tip signal.

Table 1 Experimental flow conditions and instrumentation

Fr_1	h (m)	Q (m ³ /s)	x_1 (m)	d_1 (m)	Re	Video camera	Acoustic displacement meter (ADM)	Phase-detection probe (PDP)	Simultaneous ADM & PDP
3.8	0.020	0.0179	0.83	0.0206	3.5×10^4		✓	✓	
	0.030	0.0352	1.25	0.0326	7.0×10^4		✓	✓	
	0.054	0.0820	1.25	0.057	1.6×10^5		✓	✓	
5.1	0.012	0.0160	0.50	0.012	2.1×10^4		✓		
	0.020	0.0239	0.83	0.0209	4.8×10^4	✓	✓	✓	✓
	0.026	0.0368	1.08	0.0277	7.4×10^4		✓		
	0.030	0.0461	1.25	0.0322	9.2×10^4		✓	✓	✓
	0.034	0.0552	1.42	0.0363	1.1×10^5		✓		
	0.040	0.0689	1.67	0.042	1.4×10^5		✓		✓
	0.045	0.0815	1.88	0.047	1.6×10^5		✓		
7.5	0.020	0.0347	0.83	0.0206	6.8×10^4		✓	✓	
	0.025	0.0530	1.04	0.0273	1.1×10^5			✓	
	0.030	0.0709	1.25	0.033	1.4×10^5		✓	✓	
8.5	0.020	0.0397	0.83	0.0208	8.0×10^4		✓	✓	
10.0	0.020	0.0473	0.83	0.021	9.5×10^4		✓	✓	

Notation: Fr_1 : inflow Froude number; h : inlet sluice gate opening; Q : flow rate; x_1 : mean jump toe position; d_1 : inflow depth immediately upstream the jump toe; Re: Reynolds number.

For simultaneous free-surface and two-phase flow measurements, the vertical displacement meter (S_1 in Fig. 2) was aligned over the phase-detection probe tip, while the horizontal displacement meter (S_0) was fixed when the phase-detection probe was sampled at an elevation y . A sampling rate of 5 kHz was applied to both displacement meters and phase-detection probe. The high frequency components of the phase-detection probe signal were eliminated using a low pass filtering (0 – 25 Hz).

2.2 Flow conditions

The investigations covered a range of inflow Froude numbers Fr_1 from 3.8 to 10.0. The corresponding Reynolds number was between 3.5×10^4 and 9.5×10^4 with the upstream gate opening $h = 0.02$ m. Higher Reynolds numbers up to 1.6×10^5 were achieved with larger inlet gate openings and specified inflow Froude numbers ($Fr_1 = 5.1$). The experimental flow conditions and corresponding instrumentation are summarised in Table 1.

3 RESULTS AND DISCUSSION

3.1 Long-term swing of jump position

The relative jump toe position $x-x_1$ was recorded every 5 s for 160 minutes for an inflow Froude number $Fr_1 = 5.1$ and Reynolds number $Re = 4.8 \times 10^4$. The smoothed result is shown in Figure 3(a), illustrating some major upstream migrations ($x-x_1 < 0$) followed by more gradual returns to the mean position. The time scale was significantly larger than that of the longitudinal jump toe oscillations linked with the formation of large-size vortex structures in the roller. Figure 3(a) suggests an average swing frequency about 0.004 Hz, which is supported by the power spectrum density function deduced from fast Fourier transform (Fig. 3(b)). The probability distribution of the data showed around 20% instantaneous jump toe positions recorded at the mean position ($x-x_1 = 0$). The cumulative percentages of upstream and downstream locations were 38% and 42% respectively. Note that the flume was 3.2 m long and the mean jump toe position was 0.83 m downstream the upstream sluice gate. The short flume dimension might have restricted further movement of the jump.

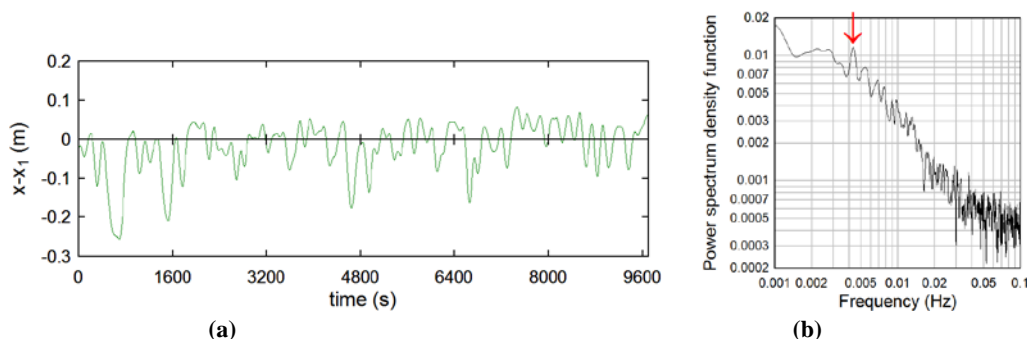


Figure 3 (a) Long-term variation of relative jump toe position; (b) Power spectrum density function for the instantaneous jump toe position. Flow conditions: $Q = 0.0239$ m³/s, $d_1 = 0.0209$ m, $x_1 = 0.83$ m, $Fr_1 = 5.1$, $Re = 4.8 \times 10^4$.

The long-term oscillations of jump position might be attributed to a process in which the energy of hydraulic jump was minimised. For example, an upstream movement of the jump tended to decrease the downstream water level to achieve lower downstream specific energy. However, because of a lesser developed boundary layer at the channel bed closer to the inlet, the inflow depth decreased slightly, leading to a temporary increase in the inflow Froude number. This tended to increase the ratio of conjugate depth d_2/d_1 according to Bélanger equation:

$$\frac{d_2}{d_1} = \frac{1}{2} \left(\sqrt{1 + 8 \times Fr_1^2} - 1 \right) \quad (3)$$

The temporary change of jump position was likely a consequence of the two opposite tendencies at

equilibrium. Since the time scale was much larger, the effect of the long-term movements can be ignored when the turbulence properties of hydraulic jump were studied.

3.2 Low-frequency turbulence: free-surface measurements

3.2.1 Free-surface fluctuations and jump front oscillations

The free-surface profile and fluctuations were measured along the channel centreline, and the longitudinal oscillations of the jump front were detected from upstream. Typical results are presented in Figure 4(a) for $Fr_1 = 5.1$ and $Re = 4.8 \times 10^4$. The time-averaged water elevations η_{fs} outlined a free-surface profile very close to the visual observations through the glass sidewall. The standard deviation of the profile fluctuations η_{fs}' were found maximum in the first half roller. Larger standard deviation was shown for the jump front oscillations in the horizontal direction (η_{toe}'). Both relative deviations of jump front oscillation (η_{toe}'/d_1) and maximum free-surface fluctuation ($(\eta_{fs}')_{max}/d_1$) exhibited some pseud-linear increase with increasing Froude number, as shown in Figure 4(b). The amplitudes of jump front oscillations was consistently higher than the free-surface fluctuations. The results in terms of free-surface fluctuations from Murzyn and Chanson (2009), Kucukali and Chanson (2008) and Mouaze et al. (2005) were plotted for comparison.

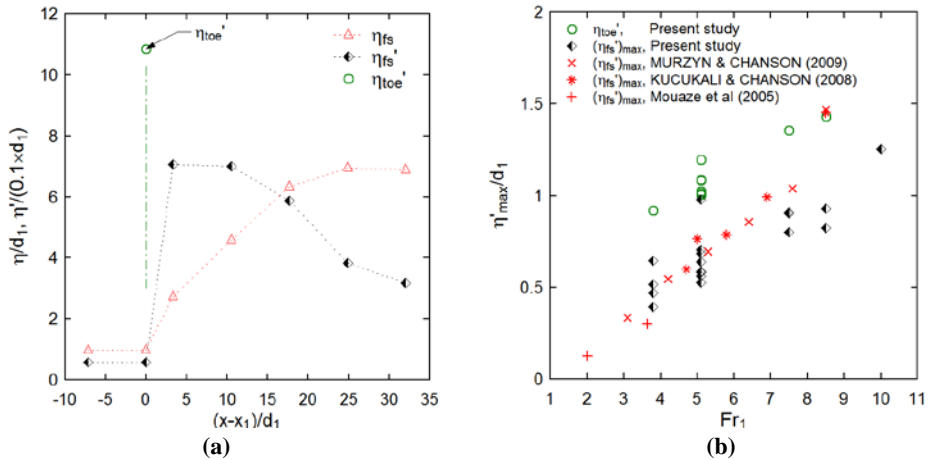


Figure 4 (a) Typical free-surface profile and fluctuations – Flow conditions: $Q = 0.0239 \text{ m}^3/\text{s}$, $d_1 = 0.0209 \text{ m}$, $x_1 = 0.83 \text{ m}$, $Fr_1 = 5.1$, $Re = 4.8 \times 10^4$; (b) Fluctuations of longitudinal jump toe position and free-surface in elevation: standard deviations of instantaneous water level data.

The characteristic frequencies of free-surface fluctuations within the roller and of longitudinal jump front oscillations were analysed based upon the power spectrum density functions of the signals. Both dominant and secondary frequencies were obtained in most situations, denoted $(F_{fs})_{dom}$ and $(F_{fs})_{sec}$ for free-surface fluctuations, and $(F_{toe})_{dom}$ and $(F_{toe})_{sec}$ for jump front oscillations respectively. The dominant free-surface fluctuation frequencies were typically between 1.2 and 3.5 Hz, whereas the dominant jump front oscillation frequencies were between 0.5 and 1.2 Hz. The dimensionless frequencies $(F \times d_1)/V_1$ are plotted in Figure 5(a) as functions of the inflow Froude number. A decrease in dimensionless dominant frequencies of free-surface fluctuations was observed with increasing Froude number and the data were best correlated by:

$$\frac{(F_{fs})_{dom} \times d_1}{V_1} = 0.163 \times \exp(-0.36 \times Fr_1) \quad (4)$$

The results are compared to the measurements of Murzyn and Chanson (2009) in terms of the free-surface fluctuation frequency F_{fs} (also using acoustic displacement meters) and visual observations of jump toe oscillation frequency F_{toe} by Zhang et al. (2013), Chanson (2010) and Murzyn and Chanson (2009). Figure 5(b) illustrates some overlapping in frequency ranges of the dominant free-surface fluctuations and secondary jump front oscillations, as well as of the secondary free-surface fluctuations

and dominant jump front oscillations. The differences in primary characteristic frequencies implied that the roller surface fluctuations in the horizontal and vertical directions were different processes. However, the processes were not independent, and the interaction was reflected by their secondary characteristic frequencies. It is noteworthy that little scale effect was noted for the free-surface fluctuations based on the experiments performed with a Froude similitude ($Fr_1 = 5.1$), whereas the dimensionless frequencies of longitudinal jump front oscillations appeared to be some larger at high Reynolds numbers, especially for $Re > 10^5$ (not shown herein).

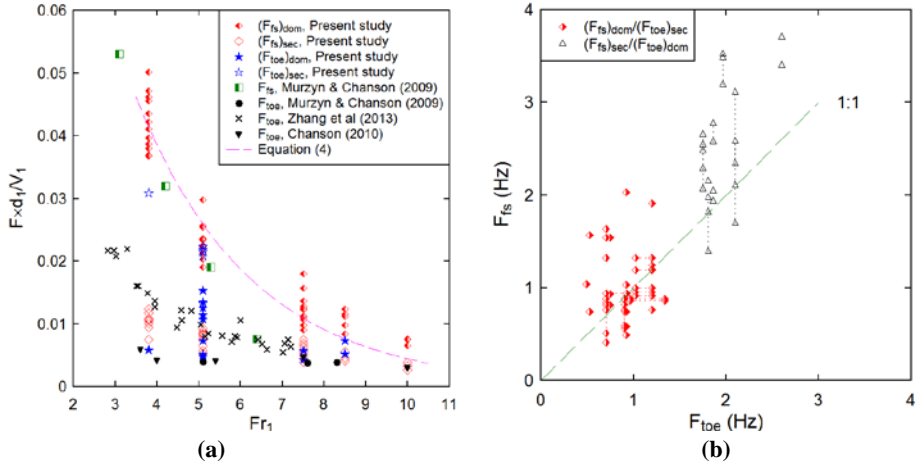


Figure 5 (a) Dimensionless characteristic frequencies of free-surface fluctuations and jump front oscillations as functions of the inflow Froude number; (b) Comparison between the ranges of dominant and secondary characteristic frequencies.

3.2.2 Roller surface deformations

The simultaneous record of the instantaneous horizontal jump front and vertical free-surface positions depicted some roller surface deformation pattern. A cross-correlation between the corresponding signals showed a marked peak in correlation coefficient, indicating a statistical trend of the change in free-surface profile. Constant results were obtained for all flow conditions: that is, at upstream of longitudinal position $x-x_1 \sim 11 \times d_1$, the water elevation above the roller increased when the jump toe moved towards upstream, and decreased when the jump toe moved towards downstream; and at downstream of $x-x_1 \sim 11 \times d_1$, the opposite trend was exhibited. The deformation pattern was sketched in Figure 6.

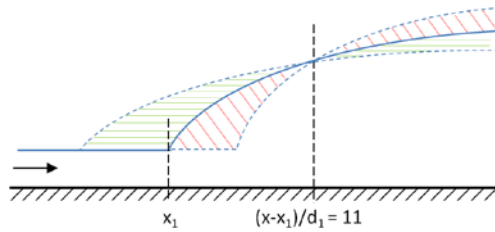


Figure 6 Trends of roller surface deformations.

3.3 High frequency turbulence: two-phase flow measurements

3.3.1 Time-averaged two-phase flow properties

Some typical distributions of the time-averaged void fraction, dimensionless bubble frequency and interfacial velocity based on the two-phase flow measurements are presented in Figure 7. The flow conditions and measurement position are detailed in the caption. The data characterised two flow regions in the roller, namely, the turbulence shear layer below and the recirculation region above a characteristic location $y = y^*$ where a local minimum void fraction was observed. In the turbulence shear layer, the void fraction distribution followed some air bubble diffusion regime with the impingement point at the jump

toe being the source, and the buoyancy effect was taken into account (Chanson, 1995). The void fraction, bubble frequency and velocity exhibited maxima at different elevations, as shown in Figure 7. In the recirculation region where negative velocity was detected, the void fraction increased monotonically to unity above the free-surface, and a secondary peak is shown in the bubble frequency.

The magnitude of maximum void fraction, bubble frequency and velocity decreased along the roller. Experimental data showed that

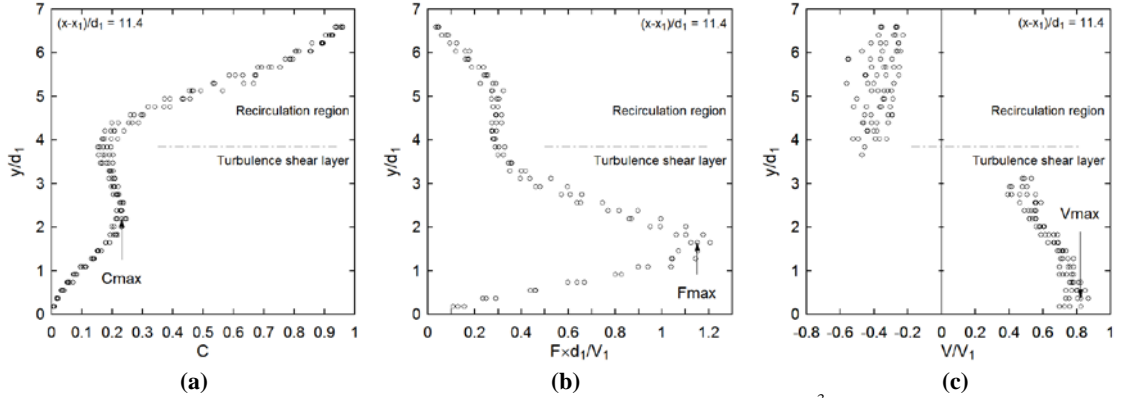


Figure 7 Time-averaged two-phase flow properties – Flow conditions: $Q = 0.0530 \text{ m}^3/\text{s}$, $d_1 = 0.0273 \text{ m}$, $x_1 = 1.04 \text{ m}$, $x-x_1 = 0.31 \text{ m}$, $Fr_1 = 7.5$, $Re = 1.1 \times 10^5$. (a) Void fraction; (b) Dimensionless bubble frequency; (c) Interfacial velocity.

$$C, \frac{F \times d_1}{V_1}, \frac{V}{V_1} \propto \exp\left(A \times \frac{x-x_1}{d_1}\right) \quad (5)$$

where A is a dimensionless factor characterising the decay rate along the roller. The present results were best correlated by:

$$C_{max} = (0.44 + 0.014 \times Fr_1) \times \exp\left[-0.9 \times \exp(-0.34 \times Fr_1) \times \left(\frac{x-x_1}{d_1}\right)\right] \quad (6)$$

$$F_{max} = \left(0.34 + 0.13 \times \frac{Re}{10^4}\right) \times \frac{V_1}{d_1} \times \exp\left[-0.5 \times \exp(-0.29 \times Fr_1) \times \left(\frac{x-x_1}{d_1}\right)\right] \quad (7)$$

$$V_{max} = V_1 \times \exp\left[-0.1 \times \exp(-0.17 \times Fr_1) \times \left(\frac{x-x_1}{d_1}\right)\right] \quad (8)$$

Equation (6) to (8) indicated that the decay rates of the maxima were related to the inflow Froude number. For a given Reynolds number, the flow with a large inflow Froude number had a large relative inertia force, and was able to advect the bubbly flow structures over a longer streamwise distance. However, it is acknowledged that the present experiments were performed with constant upstream gate openings h , and the Reynolds number differed with various Froude numbers. That is, the air diffusion and dispersion, buoyancy, flow deceleration and intensive turbulence development might be all critical to the de-aeration process. On the other hand, the quantitative level of maximum void fraction was a function of the Froude number, whereas that of maximum bubble frequency showed clearly a linear correlation to the Reynolds number. It implied that the amount of entrapped air was more likely affected by the inertia force and momentum, while the number of air bubbles was primarily determined by the shear stress in the shear layer. The elevation of maximum bubble frequency was consistently lower than the maximum void fraction and higher than the maximum velocity: $Y_{C_{max}} > Y_{F_{max}} > Y_{V_{max}}$.

3.3.2 Air entrainment flux

Air entrainment occurred at the jump toe when the inflow impinged into the roller. Further aeration and de-aeration also took place at the jump roller free-surface. The entrapped air flux was derived from the mass conservation equation of air phase based upon the void fraction and interfacial velocity measurements:

$$q_{\text{ent}} = \int_0^{Y_{90}} C \times V dy \quad (9)$$

where Y_{90} is the elevation for which the average void fraction equals 0.9. Y_{90} is considered as the upper boundary of homogeneous air-water region. In the jump roller, the air flux was calculated separately in the shear layer ($q_{\text{ent}}^{(a)} > 0$) and recirculation region ($q_{\text{ent}}^{(b)} < 0$). A definition sketch is shown in Figure 8(a), and the results are plotted in Figure 8(b) for some strong hydraulic jumps for which the flow recirculation could be clearly identified. Herein q is the specific water discharge and L_r is the length of jump roller.

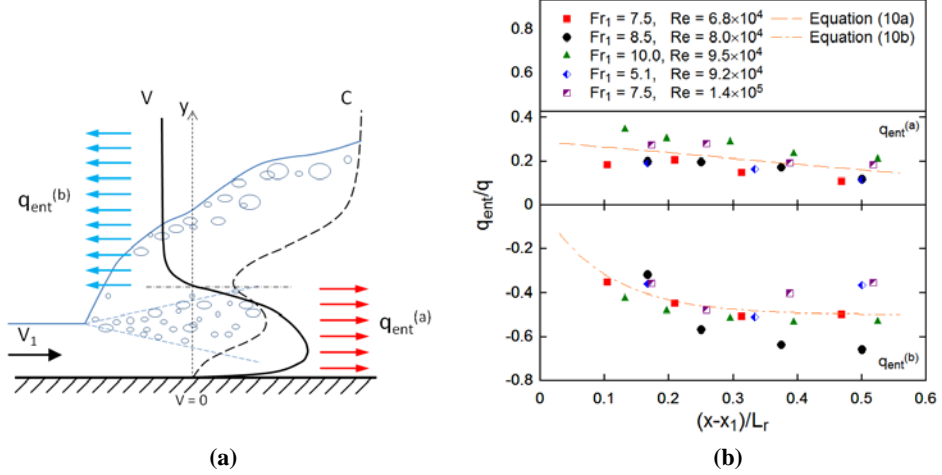


Figure 8 (a) Definition sketch of entrained and recirculating air flux; (b) Air entrainment flux in the jump roller.

The entrained air flux in the shear layer $q_{\text{ent}}^{(a)}$ was shown to decrease with increasing distance from the impingement point. The turbulence shear enhanced the dispersion of air bubbles in this region, and the bubbles were driven into the upper recirculation region by the buoyancy and centrifugal force of large vortex flow structures. In the recirculation region, the air flux was negative and its magnitude increased rapidly within $0 < x-x_1 < 0.3 \times L_r$. The average trends for all flow conditions were best correlated by Equation (10):

$$\frac{q_{\text{ent}}^{(a)}}{q} = 0.29 - 0.26 \times \frac{x-x_1}{L_r} \quad \text{for } 0 < y < y(V=0) \quad (10a)$$

$$\frac{q_{\text{ent}}^{(b)}}{q} = -0.5 \times \left[1 - \exp\left(-10 \times \frac{x-x_1}{L_r}\right) \right] \quad \text{for } y(V=0) < y < Y_{90} \quad (10b)$$

The quantitative data indicated that the recirculating air flux was greater than the entrained air flux, i.e. $|q_{\text{ent}}^{(b)}| > |q_{\text{ent}}^{(a)}|$, hence the entrained air flux in the shear layer was not the only source of the recirculating flux. It implied that the aeration rate through the roller surface was greater than the de-aeration rate. Note that Y_{90} was consistently higher than the mean free-surface elevation η_{fs} recorded by the acoustic displacement meters. Further analysis showed that about 30% of the recirculating air flux was contributed by the bubbly flow ($y(V=0) < y < \eta_{fs}$) and the rest was from the air phase in the spray and splashing free-surface region ($\eta_{fs} < y < Y_{90}$). Overall, the absolute air flux $|q_{\text{ent}}| = |q_{\text{ent}}^{(a)}| + |q_{\text{ent}}^{(b)}|$ suggested that the total air entrainment flux at the jump toe was roughly 30% of the water discharge for $5.1 < Fr_1 < 10.0$, and reached maximum at $x-x_1 = 0.3 \times L_r$ in most cases because of additional aeration at the roller surface.

3.3.3 Instantaneous air entrainment and roller surface deformations

Simultaneous measurements of the instantaneous void fraction c and free-surface positions (η_{toe} in the horizontal direction and η_{fs} in the vertical direction) characterised the interaction between the air entrainment and roller surface deformation. Although the typical bubble frequency was higher than the characteristic free-surface fluctuation and jump toe oscillation frequencies in magnitude, the signals of two-phase flow measurements were filtered to eliminate the high-frequency components, and the processed data reflected the entrainment of large amount of air bubbles. Cross-correlations between the

free-surface data and instantaneous void fraction showed maximum (or minimum) correlation coefficients $R(\eta_{\text{toe}c})_{\text{max}}$ and $R(\eta_{\text{fs}c})_{\text{max}}$ at most elevations y where the void fraction was measured. Some typical distributions of $R(\eta_{\text{toe}c})_{\text{max}}$ and $R(\eta_{\text{fs}c})_{\text{max}}$ were presented in Figure 9 together with the time-averaged void fraction C .

The void fraction and vertical free-surface fluctuations in Figure 9 were measured at longitudinal position $x-x_1 \sim 4 \times d_1$. Both $R(\eta_{\text{toe}c})_{\text{max}}$ and $R(\eta_{\text{fs}c})_{\text{max}}$ were shown positive in the lower shear layer ($y/d_1 < 1$) and negative in the recirculation region ($y > y^*$). It indicated that, when an increasing number of air bubbles were detected in the lower shear layer, the jump front moved upstream and the free-surface level increased (corresponding to an upstream movement of jump toe as illustrated in Fig. 6), while they shifted in the opposite directions when the air phase increased in the recirculation region. In the region $1 < y/d_1 < y^*/d_1$ where the major entrained air was advected downstream, the maxima exhibited opposite signs, i.e. $R(\eta_{\text{toe}c})_{\text{max}} < 0$ and $R(\eta_{\text{fs}c})_{\text{max}} > 0$. It corresponded to a downstream movement of jump front and increase in free-surface elevation when a large amount of air was entrapped. The motions of the roller surface were the results of high-aerated large vortices detachment from the jump toe and corresponding flow bulking. This instantaneous roller surface deformation pattern was not revealed by the statistical coupling between the free-surface fluctuations (Fig. 6). Overall, the results suggested different types of surface deformation for a detected change in void fraction within different parts of the jump roller.

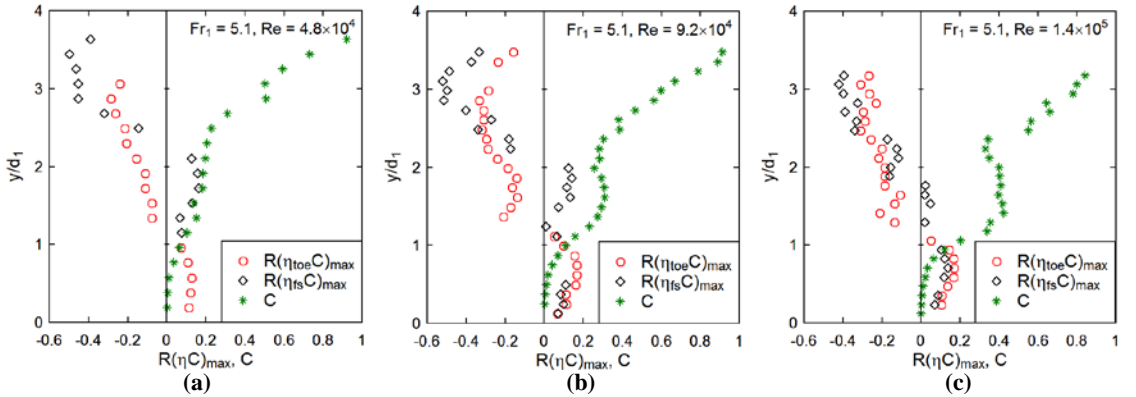


Figure 9 Maximum cross-correlation coefficients between free-surface fluctuations η_{toe} and η_{fs} and instantaneous void fraction c measured at $(x-x_1)/d_1 = 4$ – Flow conditions: (a) $Q = 0.0239 \text{ m}^3/\text{s}$, $d_1 = 0.0209 \text{ m}$, $x_1 = 0.83 \text{ m}$, $x-x_1 = 0.083 \text{ m}$, $Fr_1 = 5.1$, $Re = 4.8 \times 10^4$; (b) $Q = 0.0461 \text{ m}^3/\text{s}$, $d_1 = 0.0322 \text{ m}$, $x_1 = 1.25 \text{ m}$, $x-x_1 = 0.125 \text{ m}$, $Fr_1 = 5.1$, $Re = 9.2 \times 10^4$; (c) $Q = 0.0689 \text{ m}^3/\text{s}$, $d_1 = 0.042 \text{ m}$, $x_1 = 1.67 \text{ m}$, $x-x_1 = 0.167 \text{ m}$, $Fr_1 = 5.1$, $Re = 1.4 \times 10^5$.

Discussion

The presented unstationary flow features with various frequency ranges existed in a hydraulic jump at the same time. For a study of the turbulence properties, the effect of long-term motions can be ignored, while both low- and high-frequency fluctuations contributed to the turbulence development. For example, the turbulence intensity in the bubbly flow region was calculated with Equation (2) based on the two-phase flow measurements, and was expected to reflect the velocity fluctuations in a high-frequency level. However, the low-frequency motions induced some very large turbulence intensities especially in the recirculation region where the free-surface deformations were comparably important as the turbulence. Some triple decomposition analysis by Felder and Chanson (2012) showed that the high-frequency component (greater than 10 Hz) of the turbulence intensity remained in a reasonable range ($Tu = v'/V_1 \sim 1.2 \pm 0.6$, $Fr_1 = 7.1$ & 7.5) through a cross-section of the roller. It indicated that the effect of low-frequency component (0.33 to 10 Hz) should be specified and excluded. The frequency thresholds for triple decomposition in Felder and Chanson (2012) were determined based on some sensitivity study. In the present study, detailed physical basis was provided for the choice of the low- and high-frequency ranges.

4 CONCLUSIONS

The unstationary flow properties of hydraulic jumps were investigated in three time scale levels: the long-term jump position shifts with a characteristic frequency smaller than 0.1 Hz, the low-frequency free-surface fluctuations between 0.1 and 10 Hz, and the high-frequency two-phase flow turbulence

greater than 10 Hz. A 160-minute successive observation of jump position showed the average shift frequency of 0.004 Hz and the displacements roughly between $-14 < (x-x_1)/d_1 < 5$. The slow pseudo-periodic motion was attributed to an energy-minimisation process at equilibrium. The effect of this motion can be ignored when the flow is studied in much smaller time scales. The free-surface fluctuations were measured non-intrusively in vertical and horizontal directions along the centreline. The free-surface profiles were outlined and maximum vertical fluctuations were noted in the first half roller. The horizontal fluctuations associated with the longitudinal jump toe oscillations showed larger amplitudes than the vertical fluctuations, and both fluctuation levels increased with increasing inflow Froude number of the flow. The characteristic frequencies showed both dominant and secondary frequencies for the horizontal and vertical fluctuations. A frequency range of 0.5 to 1.2 Hz was obtained for the dominant horizontal and secondary vertical fluctuations, whereas the dominant vertical and secondary horizontal motions were between 1.2 and 3.5 Hz. The overlapping frequency ranges implied different regimes for the jump toe oscillations and free-surface fluctuations but some interaction in between. The coupling between the two motions revealed a statistical roller surface deformation pattern that differed at upstream and downstream of the position $x-x_1 \sim 11 \times d_1$. The two-phase flow properties were measured with an intrusive phase-detection probe. The time-averaged void fraction, bubble frequency and interfacial velocity profiles were obtained in the roller. The air bubble diffusion process along the roller shear layer was related mainly to the inflow Froude number, while the magnitude levels of void fraction and bubble frequency were affected by the Froude and Reynolds numbers respectively. The entrained and recirculating air fluxes were calculated, showing different aeration/de-aeration tendencies in the shear layer and recirculation region. The air entrapment rate at the jump toe was estimated to be about 30% of the water discharge. Simultaneous measurements of the instantaneous void fraction and free-surface fluctuations showed different relationships between the air entrainment and surface deformations when the entrapped air was detected in different regions of jump roller. The contribution of the low- and high-frequency fluctuations to the turbulence intensity was discussed lastly.

ACKNOWLEDGEMENT

The authors thank Stefan Felder for his data acquisition and processing programs that efficiently facilitated the physical modelling study. The financial support of the Australian Research Council (Grants DPDP0878922 & DP120100481) is acknowledged.

References

- Chachereau Y. and Chanson H., 2011a. Free-surface fluctuations and turbulence in hydraulic jumps. *Experimental Thermal and Fluid Science*, 35(6), 896-909.
- Chachereau Y. and Chanson H., 2011b. Bubbly flow measurements in hydraulic jumps with small inflow Froude numbers. *International Journal of Multiphase Flow*, 37(6), 555-564.
- Chanson H., 1995. Air entrainment in two-dimensional turbulent shear flows with partially developed inflow conditions. *Journal of Multiphase Flow*, 21(6), 1107-1121.
- Chanson H., 2007. Dynamic similarity and scale effects affecting air bubble entrainment in hydraulic jumps. *Proceedings of 6th International Conference on Multiphase Flow ICMF 2007*, Leipzig, Germany, July 9-13.
- Chanson H., 2010. Convective transport of air bubbles in strong hydraulic jumps. *International Journal of Multiphase Flow*, 36(10), 798-814.
- Chanson H. and Brattberg T., 2000. Experimental study of the air-water shear flow in a hydraulic jump. *International Journal of Multiphase Flow*, 26(4), 583-607.
- Chanson H. and Carosi G., 2007. Advanced post-processing and correlation analyses in high-velocity air-water flows. *Environmental Fluid Mechanics*, 7(6), 495-508.
- Chanson H. and Toombes L., 2002. Air-water flows down stepped chutes: turbulence and flow structure observations. *International Journal of Multiphase Flow*, 28(11), 1737-1761.
- Felder S. and Chanson H., 2012. Air-water flow measurements in instationary free-surface flows: a triple decomposition technique. *Research report No. CH85/12*, School of Civil Engineering, The University of Queensland, Brisbane, Australia, 144 pages.
- Kucukali S. and Chanson H., 2008. Turbulence measurements in hydraulic jumps with partially-developed inflow conditions. *Experimental Thermal and Fluid Science*, 33(1), 41-53.
- Mossa M., 1999. On the oscillating characteristics of hydraulic jumps. *Journal of Hydraulic Research*, 37(4), 541-558.
- Mouaze D., Murzyn F. and Chaplin J., 2005. Free surface length scale estimation in hydraulic jumps. *Journal of*

- Fluids Engineering, 127(6), 1191-1193.
- Murzyn F., Mouaze D. and Chaplin J., 2005. Optical fibre probe measurements of bubbly flow in hydraulic jumps. *International Journal of Multiphase Flow*, 31(1), 141-154.
- Murzyn F. and Chanson H., 2009. Experimental investigation of bubbly flow and turbulence in hydraulic jumps. *Environmental Fluid Mechanics*, 9(2), 143-159.
- Zhang G., Wang H. and Chanson H., 2013. Turbulence and aeration in hydraulic jumps: free-surface fluctuation and integral turbulent scale measurements. *Environmental Fluid Mechanics*, 13(2), 189-204. DOI 10.1007/s10652-012-9254-3.